LIFE SCIENCES

Bottom-up assembly of biomedical relevant fully synthetic extracellular vesicles

Oskar Staufer[1,2,3,4]*, Franziska Dietrich[1,2], Rahul Rimal[5], Martin Schröter[1,2], Sebastian Fabritz[6], Heike Boehm[1,2,4], Smriti Singh[5], Martin Möller[5,4], Ilia Platzman[1,2,3]*, Joachim Pius Spatz[1,2,3,4]*

Extracellular vesicles (EVs) are fundamental for intercellular communication and influence nearly every process in cell physiology. However, because of their intricate molecular complexity, quantitative knowledge on their signaling mechanisms is missing, particularly impeding their therapeutic application. We used a complementary and quantitative engineering approach based on sequential synthetic bottom-up assembly of fully functional EVs with precisely controlled lipid, protein, and RNA composition. We show that the functionalities of synthetic EVs are analogous to natural EVs and demonstrate their programmable therapeutic administration for wound healing and neovascularization therapy. We apply transcriptome profiling to systematically decode synergistic effects between individual EV constituents, enabling analytical dissection and a fundamental understanding of EV signaling.

INTRODUCTION

Intercellular signaling is fundamental for the vital functioning of multicellular organisms. In this context, the seminal discovery of extracellular vesicle (EV)–based intercellular communication has revolutionized our understanding of cell-to-cell signaling and has lately raised considerable diagnostic and therapeutic interest. EVs, such as exosomes, oncosomes, and microvesicles, present membrane-associated proteins and shuttle (epi-)genetic regulatory elements like microRNAs (miRNAs) between distant cells, thereby affecting nearly every facet of cell physiology including, but not limited to, migration (*1*), proliferation (*2*), and differentiation (*3*). Therefore, attaining a fundamental understanding of EV-mediated intercellular communication mechanisms is a compelling goal also for developing EV-based theranostics (*4*, *5*). However, the elaborate and error-prone procedures required for EV isolation, purification, and characterization from natural sources as well as their extensive molecular complexity have been a hurdle for understanding the associated signaling events.

Recently, the charge-mediated assembly of giant unilamellar vesicles (GUVs) from small unilamellar vesicle (SUV) precursors inside water-in-oil (w/o) droplets by microfluidic technology (*6*, *7*) as well as bulk emulsification (*8*) was reported and applied for vesicle-cell interaction studies (*9*, *10*). The microfluidic approach has the advantage to control the size of the vesicles rigorously (*10*) and allows quantitative integration of membrane proteins (*6*). This is pivotal concerning the lateral mobility of proteins in the vesicle membrane (*11*) and crucial for vesicle-mediated clustering of cell membrane receptors (*12*), which regulates functions and signaling at the cellular level (*13*). Eventually, the bulk emulsification method enables fast formation of larger amounts of these vesicles, including vesicles in the sub-micrometer size range, as suitable for the construction of EV mimetic materials but with slightly increased polydispersity (*8*). Therefore, this high-throughput charge-mediated vesicle assembly technology allows extremely high encapsulation efficiencies of biomolecules and the incorporation of integral and peripheral membrane proteins. Moreover, it offers precise quantitative control over vesicle composition and, therefore, over the biochemical and biophysical phenotype of the vesicles. Last, the resulting synthetically assembled vesicles in many parts closely resemble naturally occurring lipid carriers such as EVs. In particular, bottom-up assembly of EV mimics enables stepwise quantitative loading of EVs with different important molecular signaling compounds, which enables exquisite control over their physicochemical properties, mechanical and chemical stability, intracellular admission, and manipulability (*14*). These fully synthetic EVs (fsEVs) accurately mirror the complex molecular architecture of EV particles exclusively from artificial precursors (Fig. 1A). FsEVs offer quantitatively controlled minimalistic models to study and engineer fundamental biophysical and biochemical mechanisms of EV signaling. Moreover, as fsEVs are not subjected to intrinsic biological fluctuations, they might provide a more secure therapy option if successfully triggering EV-equivalent therapeutic responses.

RESULTS

Droplet-based assembly of fsEV scaffolds

Lipids are the major scaffolding components of EVs and pivotal for their signaling capabilities. Therefore, we aimed to assemble fsEVs by charge-mediated formation inside w/o droplets produced by mechanical emulsification from synthetic lipids with compositions that resemble those found in natural EVs. Although it is technically possible to integrate an almost unrestricted selection of lipid types into fsEV membranes (*8*), we chose a lipid formulation (cholesterol:SM:DOPC:DOPS:DOPE:DOPG:PA:DAG:DOPI 43:16:15:11:6:5:2:1:1) that incorporates the most abundant EV lipid types and classes (*15*). We used quantitative electrospray ionization tandem mass spectrometry (MS) to verify the lipid composition of the formed fsEVs, demonstrating that they can be constructed using the desired ratio (see fig. S1). By cryo–transmission electron microscopy (cryo-TEM), we verified the unilamellar nature of fsEVs (see fig. S2). To assess structural similarities between fsEVs and natural

---

[1]Department for Cellular Biophysics, Max Planck Institute for Medical Research, Jahnstraße 29, 69120 Heidelberg, Germany. [2]Institute for Molecular Systems Engineering (IMSE), Heidelberg University, 69120 Heidelberg, Germany. [3]Max Planck-Bristol Center for Minimal Biology, University of Bristol, 1 Tankard's Close, Bristol BS8 1TD, UK. [4]Max Planck School Matter to Life, Jahnstraße 29, 69120 Heidelberg, Germany. [5]DWI-Leibniz-Institute for Interactive Materials, Forckenbeckstrasse 50, 52056 Aachen, Germany. [6]Department for Chemical Biology, Max Planck Institute for Medical Research, Jahnstraße 29, D-69120 Heidelberg, Germany.
*Corresponding author. Email: oskar.staufer@mr.mpg.de (O.S.); ilia.platzman@mr.mpg.de (I.P.); spatz@mr.mpg.de (J.P.S.)

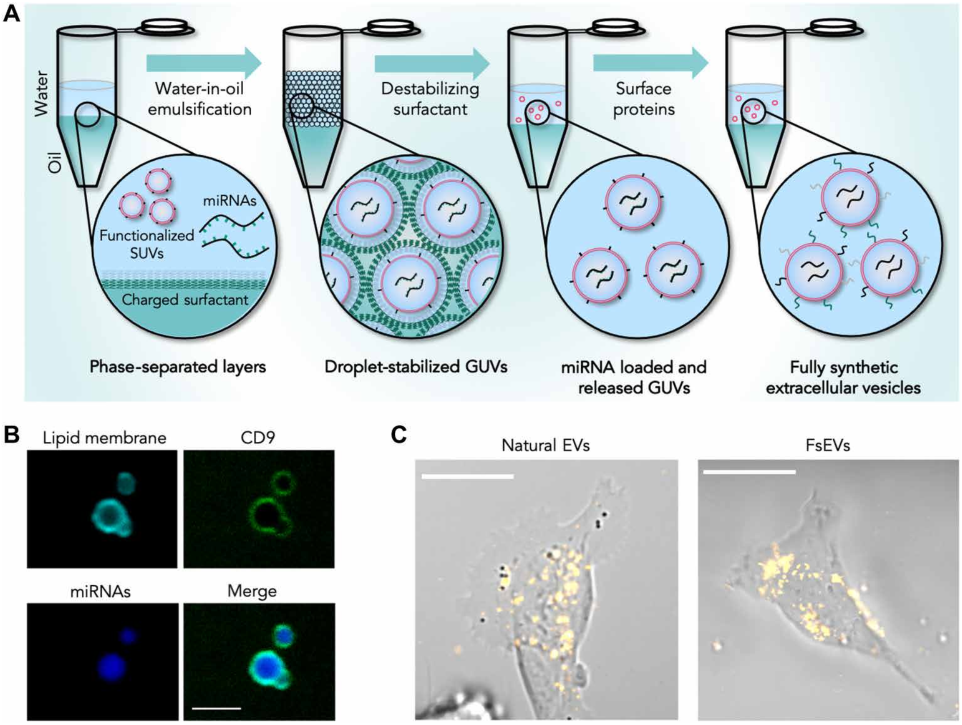

Fig. 1. Bottom-up assembly of fsEVs inside w/o emulsions. (**A**) Schematic illustration of the fsEV formation process inside w/o droplet compartments produced by mechanical emulsification. miRNA-containing lipid vesicles are formed on the periphery of water droplets from SUV precursors for subsequent decoration with surface proteins. (**B**) Confocal microscopy images of fsEVs labeled with Liss Rhod PE–labeled fluorescent lipids (lipid membrane), Alexa Fluor 488–labeled CD9 (CD9), and Hoechst 33342–labeled miRNAs (hsa-miR-21, hsa-miR-124, hsa-miR-125, hsa-miR-126, hsa-miR-130, and hsa-miR-132). Scale bar, 2 μm. (**C**) Representative fluorescence confocal microscopy images of human dermal fibroblasts incubated for 24 hours with DiI (1,1′-dioctadecyl-3,3,3′,3′-tetramethylindocarbocyanine perchlorate)–labeled natural EVs isolated from K562 media (left) or incubated for 24 hours with fluorescent fsEVs. Scale bars, 20 μm.

EVs, we compared respective samples by TEM (see fig. S3). Towards this end, we analyzed K562 EVs isolated by differential centrifugation as well as K562 EVs obtained from a commercial distributer and found considerably fewer contaminating aggregates and nonvesicular particles in the fsEV preparations underscoring their purity and definition. To evaluate the biophysical similarity between fsEVs and natural EVs, we performed dynamic light scattering (DLS) analysis. We found that the fsEV size can be customized by adjusting the emulsification shear stress, allowing the creation of fsEV with radii between 292 nm (±12 nm, $n = 3$ technical replicates; produced by 30-s emulsification at 30,000 rpm) and 627 nm (±15 nm, $n = 3$ technical replicates; produced by 30-s emulsification at 14,000 rpm) and a zeta potential of fsEVs of −12.3 mV (±0.7 mV, $n = 3$ technical replicates). FsEV size and zeta potential are therefore in the same range as reported for natural EVs (*16*, *17*). Moreover, these values are in the same range as measured for commercial K562 EVs (468 ± 199 nm and −11.8 ± 0.9 mV, $n = 3$ technical replicates), and to EVs, we isolated from conditioned K562 media (240 ± 32 nm and −11.3 ± 0.5 mV, $n = 3$ technical replicates). To assess the stability of fsEVs compared to natural K562 EVs, we measured changes in polydispersity index (PDI) of both vesicle types over a period of 20 days by DLS. We found that the PDI of fsEVs did not significantly increase in this time period, while for natural EVs we found an increase by ~50%. This underscores the stability of fsEV preparations (see fig. S4). Research on EVs has been greatly hampered by batch-to-batch variations and the presence of impurities introduced during isolation and purification procedures (*18*, *19*). FsEVs, in turn, can be assembled from well-defined synthetic constituents in vitro, thereby circumventing the introduction of impurities by cellular production techniques. Our results confirm that homogeneous fsEVs can be assembled from individually adjustable synthetic lipid precursors matching the lipid composition and biophysical characteristics of natural EVs.

The main physiological function of EVs with relevance to therapeutic potential is commonly attributed to their RNA, in particular miRNA, cargo, as well as the membrane proteins and the receptor ligands on their surface. To demonstrate the therapeutic potential of fsEVs, we aimed to rebuild fibrocyte-derived EVs with their main miRNA (hsa-miR-21, hsa-miR-124, hsa-miR-125, hsa-miR-126, hsa-miR-130, and hsa-miR-132) and protein components (CD9, CD63, and CD81). These EVs have been described to promote diabetic wound healing and are now being explored for clinical application (*20*). We constructed fsEVs with a size of 333 nm (±32 nm) containing synthetic double-stranded miRNA mimics of the fibrocyte EV miRNAs at naturally occurring concentrations (750 pg/10^{12} vesicles) (*21*) by mixing the respective RNAs with the initial SUV solution used for droplet production (see Fig. 1A). We approximated the number of miRNA molecules inside fsEVs by measuring the total encapsulated miRNAs, fsEV concentration, and fsEV size via gel electrophoresis, nanoparticle tracking analysis, and DLS, respectively (see fig. S5). We found, on average, 54 ± 5.6 miRNA molecules per fsEV, which is in good agreement with previous estimations of the active RNA content in EVs (*21*). Following the release of the nascent vesicles into an aqueous solution, fsEV membranes were decorated at a 1:200 protein to lipid ratio with recombinant second extracellular domains of histidine-tagged human tetraspanins CD9, CD63, and CD81 via NTA(Ni^{2+}) lipids. Note that similar protein to lipid ratios have been described for natural EVs (*22*), and previous studies have also demonstrated that the second extracellular loop of tetraspanins is the key functional element and prevalent for the protein activity (*23*, *24*). Confocal microscopy analysis showed correct assembly of respective fsEVs by revealing luminal distribution of the miRNAs and peripheral distribution of Alexa Fluor 488–labeled CD9, overlapping with Liss Rhod PE fluorescence of the lipid bilayer (Fig. 1B). To show that the use of bio-orthogonal NTA(Ni^{2+}) surface chemistry allows to precisely control the fsEV membrane protein composition, we performed denaturating polyacrylamide gel electrophoresis (PAGE) analysis. We found that fsEVs assembled with EV marker proteins produced a more defined band pattern compared to the protein profiles of natural EVs (see fig. S6). Moreover, this pattern showed higher batch-to-batch reproducibility compared to the natural EVs, demonstrating that fsEVs outperform EV isolates from natural sources in terms of purity and reproducibility. These fsEVs, designed for wound-healing therapy, were also readily internalized by human dermal fibroblasts and showed comparable uptake and intracellular distribution to natural EVs (Fig. 1C and fig. S7). In addition, when incubated with human keratinocytes [HaCaT cells; (*25*)], a charge-dependent intracellular uptake was observed (see movie S1 and fig. S8). In summary, this demonstrates the accurate bottom-up assembly of miRNA-loaded and protein-decorated fsEVs, which mimic the structure of natural EVs through a step-by-step amalgamation of biomolecules to form precisely defined particles according to a bioinspired building plan.

Bottom-up assembly of wound-healing fsEVs

When studying the therapeutic potential of EVs secreted by human circulating fibrocytes, Geiger *et al.* (*20*) observed three prominent cellular responses: (i) increased proliferative and (ii) acceleration of the collective migratory behavior of keratinocytes as well as (iii) enhanced collagen deposition by dermal fibroblasts, ultimately promoting in vivo wound closure (*20*). To assess whether fsEVs display analogous functionalities, we first analyzed their pro-proliferative effect on HaCaT keratinocytes. In addition, to systematically decipher the functional contribution of the individual fsEV components, we constructed fsEVs decorated with a single tetraspanin or combinations of them but lacking miRNAs. This further highlights one of the key advantages of EV assembly in a bottom-up approach: It allows the engineering of individually adjustable vesicle compositions, which not only is more straightforward compared to genetic engineering of EVs in living cells but also allows to create vesicle compositions hardly producible by cells (*26*). Assessing keratinocyte proliferation by measuring total DNA content in the cultures (*27*) and by counting mitotic figures by nuclear staining 48 hours of fsEV treatment revealed a pro-proliferative effect (Fig. 2A and fig. S9, A and B). The copresentation of combinations of tetraspanins led to a synergistic effect on proliferation. The pro-proliferative effect was most pronounced when all three tetraspanins were copresented, inducing a more than twofold increase compared to cultures treated with naive vesicles. The exact signaling routes of EV-presented tetraspanins are yet to be clarified, but CD9, CD63, and CD81 have been shown to interact with a plethora of cell surface receptors including integrin proteins (*28*). Here, in particular, the interaction of CD81 with integrin β_1 has been shown to influence proliferation (*29*), which is further supported by our transcriptome analysis (see RNA sequencing results). These results prove that presenting the second extracellular domain of CD9, CD63, and CD81 on fsEVs is sufficient to obtain a pro-proliferative effect on keratinocytes.

Next, we evaluated the contribution of single miRNAs to the pro-proliferative effect observed by Geiger *et al.* (*20*) Toward this end, we produced fsEVs decorated with all three tetraspanins and loaded with miRNA mimics of hsa-miR-21, hsa-miR-124, hsa-miR-125, hsa-miR-126, hsa-miR-130, and hsa-miR-132 (50 nM each) (Fig. 2B and fig. S9C). We found that every single miRNA enhanced proliferation to a different extent, but a strong pro-proliferative effect was observed for fsEVs loaded with a combination of all six miRNAs (2.5-fold compared to unloaded but tetraspanin decorated fsEVs). All miRNAs described in the fibrocyte-derived exosomes and applied in our study have been reported to regulate the proliferation of different cell types. For instance, the highly conserved miR-125 targets a diverse number of genes like matrix metalloproteases and members of the Bcl-2 family through which it can affect proliferation (*30*). Our results demonstrate that fsEVs can act as appropriate carriers to convey miRNA-based regulatory information, thereby reconstituting a central mechanism of EV signaling.

To assess the effect of fsEVs on epithelial migration, we performed in vitro cell exclusion wound-healing assays on collectively migrating keratinocyte monolayers treated with fsEVs for 24 hours (Fig. 2C). By quantifying the cell-free area 16 hours after removal of the exclusion inserts, we found that fsEVs are able to promote collective keratinocyte migration (Fig. 2D). As observed for the pro-proliferative effect, copresentation of all three tetraspanins on the fsEV surface produced a stronger enhancement of collective cell migration compared to individual tetraspanin presentation. Moreover, when compared to treatment with fsEVs presenting only CD9, CD63, and CD81, the incorporation of miRNA mimics effectively amplified the promigratory behavior (Fig. 2E). A fundamental conceptual advancement provided by the fsEV technology lays in their defined character, allowing to systematically vary their quantitative composition to explore holistic effects. In this regard, the fsEV composition can be quantitatively engineered to optimized their functional performance. To exemplify this, we first investigated the impact of miRNA stoichiometry on in vitro keratinocyte migration, focusing on hsa-miR-132, and found that equimolar incorporation of this miRNA and the other five miRNAs shows the highest in vitro wound closure (Fig. 2F). This could indicate that specific ratios between miRNAs need to be kept to achieve proper EV signaling, which has been proposed earlier but not experimentally validated due to a lack of appropriate engineering technologies (*31*). To showcase this engineering approach on the protein level, we systematically varied the CD81 concentration coupled to the fsEVs with respect to CD9 and CD63. We found that a significantly increased migratory phenotype is already reached at an approximately 1:3:3 CD81:CD9:CD63 ratio (Fig. 2G). It also highlights how fsEV engineering can provide quantitative insights into EV signaling mechanisms. Most of the applied miRNAs regulate fundamental pathways related to the wound-healing processes (*20*). For instance, miR-21 promotes keratinocyte migration by regulation of TIMP3 and TIAM1 (*32*). Thus, alongside proliferation, the developed fsEVs can also increase collective migration of keratinocytes.

Next, we assessed pro–collagen-Iα deposition by dermal fibroblasts (BJ cells) using enzyme-linked immunosorbent assays (ELISAs)

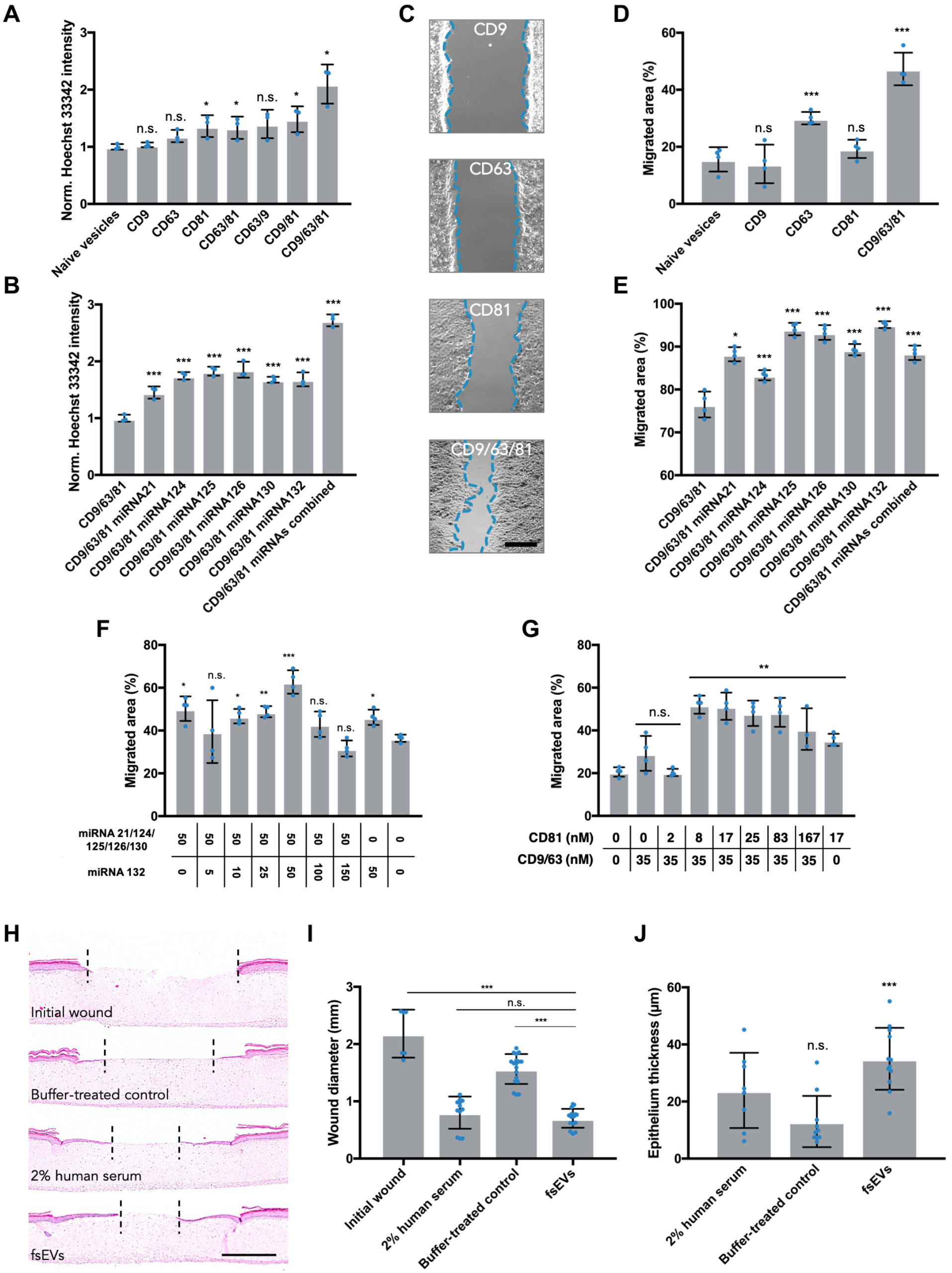

Fig. 2. Bottom-up assembly of wound-healing fsEVs. (**A** and **B**) Fluorescence intensity analysis of Hoechst 33342–stained HaCaT keratinocytes after 48-hour treatment with fsEV variants. Results are shown as means ± SD; $n = 3$ technical replicates. (**C**) Phase-contrast images of cell exclusion wound-healing assays with HaCaT monolayers after 16 hours of migration. Scale bar, 185 μm. (**D** and **E**) Quantification of exclusion wound-healing assays of HaCaT monolayers treated for 24 hours with fsEVs. Results are shown as means ± SD; $n = 4$ wound sites. (**F**) Quantification of wound-healing assays of HaCaT monolayers treated for 24 hours with fsEV variants containing varying hsa-miR-132 concentrations and the second extracellular domains of CD9, CD63, and CD81. Results are shown as means ± SD; $n = 4$ artificial wound sites. (**G**) Quantification of in vitro wound-healing assays of HaCaT monolayers treated for 24 hours with fsEVs presenting varying ratios of CD81 to CD9 and CD63. Results are shown as means ± SD; $n = 4$ artificial wound sites. (**H**) Representative histological sections of wounded organotypic human skin models. Treatments as indicated for 48 hours. Scale bar, 1 mm. (**I**) Quantification of epidermal wound-bed closure of organotypic skin models from (H) treated with 2% human serum (positive control), buffer (negative control), or fsEVs loaded with all miRNA mimics and presenting second extracellular domains of human CD9, CD63, and CD81. Results are shown as means ± SD; minimum of six individual sections per condition. (**J**) Quantification of recovered epidermal layer thickness from (H). $^{*}P < 0.01$, $^{**}P < 0.001$, and $^{***}P < 0.0001$, two-tailed *t* test; n.s., not significant to first treatment group in graph.

after incubation with fsEVs for 24 hours (fig. S10). Although our efforts to decode the individual effects of single miRNAs revealed no significant differences, a higher collagen deposition was obtained by treatment with fsEVs containing all six miRNAs and tetraspanins. Thus, the in vitro assembled vesicles, like their natural doppelgangers, comprise the ability to boost three of the most fundamental processes critical for wound healing: proliferation, migration, and collagen deposition.

Last, to assess the ability of fsEVs to promote regeneration of wounded skin, we treated organotypic full-thickness skin models (Fig. 2H) from human donors by applying fsEVs on a punched wound site for 48 hours. Closure of the 3-mm epidermal wound was assessed by quantifying epithelial wound-bed size in hematoxylin and eosin (H&E)–stained histological samples. We found that, as compared to buffer-treated controls, fsEVs substantially augmented the healing with no significant difference to the positive control (Fig. 2I). Moreover, the regenerated epidermal layer thickness was significantly increased to the buffer-treated controls, demonstrating that the healing process is not only faster but presumably also of higher grade (Fig. 2J). Together, these data show that the bottom-up design and assembly of fsEVs using a droplet-stabilized approach can produce artificial EVs with analog therapeutic potential to natural EVs. We anticipate that this breakthrough technology will significantly advance the applicability of EV-like structures in a multitude of clinical settings.

Functional mechanisms of fsEV signaling

To elucidate the functional mechanisms of the wound-healing EVs and to correlate the specific fsEV-mediated macroscopic phenotypic effects observed above to specific transcriptomic changes and activated biochemical pathways, we performed RNA sequencing transcriptome analysis of fsEV-treated keratinocytes cultures. Toward this end, we compared cultures treated with fsEVs harboring all six miRNA mimics and the three recombinant tetraspanins to untreated cultures and to cultures treated with the respective soluble compounds (i.e., the same concentration of miRNAs and proteins added to the cells but without lipid vesicles). We found 173 differentially expressed genes (DEGs) between untreated and fsEV-treated cells (Fig. 3A and table S1). When analyzing the soluble compounds, only five DEGs were found, indicating that the EV components only unfold their full signaling potential when presented or incorporated on a vesicle (table S2). Pathway enrichment analysis (PEA) of these

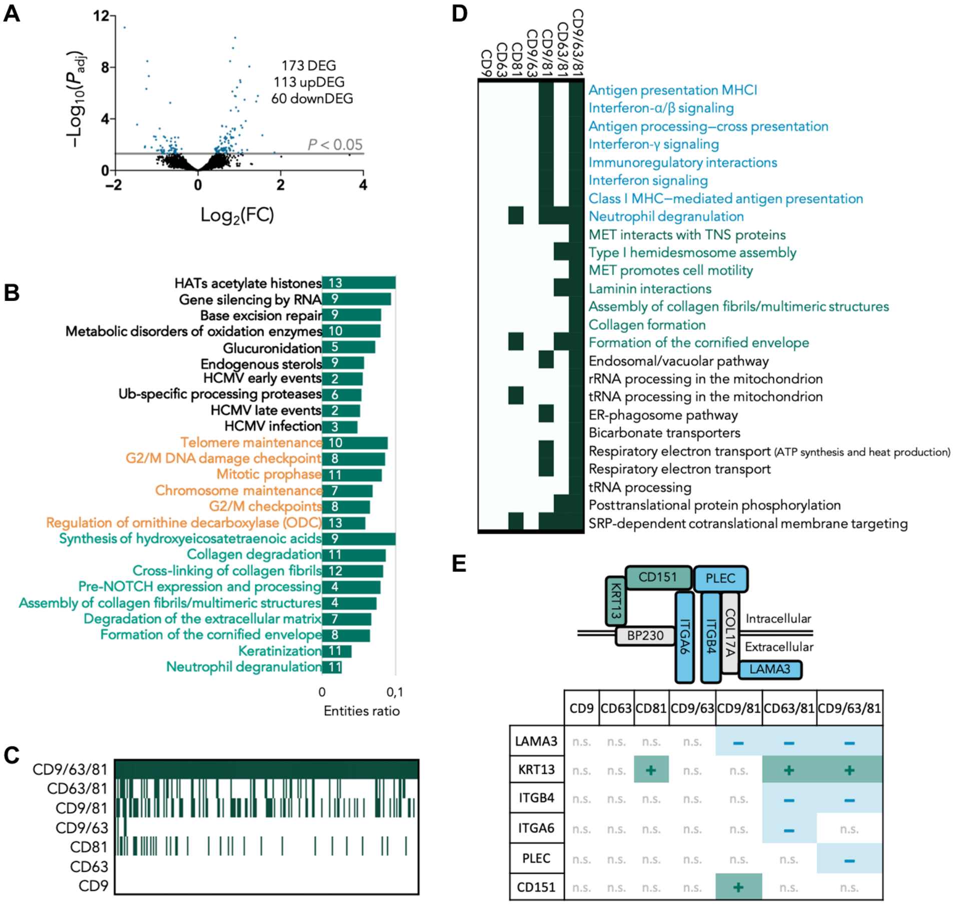

	CD9	CD63	CD81	CD9/63	CD9/81	CD63/81	CD9/63/81
LAMA3	n.s.	n.s.	n.s.	n.s.	–	–	–
KRT13	n.s.	n.s.	+	n.s.	n.s.	+	+
ITGB4	n.s.	n.s.	n.s.	n.s.	n.s.	–	–
ITGA6	n.s.	n.s.	n.s.	n.s.	n.s.	–	n.s.
PLEC	n.s.	n.s.	n.s.	n.s.	n.s.	n.s.	–
CD151	n.s.	n.s.	n.s.	n.s.	+	n.s.	n.s.

Fig. 3. RNA sequencing transcriptome profiling of fsEV-treated keratinocytes. (**A**) Volcano plot of RNA sequencing analysis of keratinocytes treated with fsEVs. Single DEGs above the $P_{\mathrm{adj}} < 0.05$ threshold (gray line) are highlighted in blue. Summary of up- and down-regulated DEGs is given in the upper-right corner. FC, fold change. (**B**) Top 25 enriched pathways based on Reactome pathway enrichment analysis of fsEV-treated keratinocytes. Results are sorted by entity ratio (entities present in the DEG list/total entities in the pathway). Numbers in each row indicate the amount of detected DEGs in the respective pathways. Pathways highlighted in orange are associated with cell cycle progression, and pathways highlighted in green are associated with cell migration, cell adhesion, extracellular matrix remodeling, or wound healing, respectively. (**C**) Binary heatmap of overlapping DEGs between keratinocytes treated with fsEVs of different tetraspanin combinations. Each column represents one of the 231 DEGs found in cells treated with fsEVs presenting CD9, CD63, and CD81. DEGs are marked in green. (**D**) Binary heatmap of the top 25 enriched pathways by keratinocyte treatment with fsEVs presenting CD9, CD63, and CD81 and the respective overlapping enriched pathways for treatment with vesicles of other tetraspanin combinations. Significantly ($P < 0.05$) enriched pathways are marked in green. Pathways associated with immune regulation and cell motility are highlighted in blue and green, respectively. (**E**) Schematic illustration of a type I hemidesmosome and summary of associated DEGs in fsEV-treated keratinocytes with different tetraspanin combinations. Up- and down-regulated hemidesmosome genes are indicated with + and –, respectively. n.s., no significant differential expression in the respective treatment condition.

DEGs revealed that fsEVs distinctly affect several cellular processes of fundamental importance for proper wound healing, including cell cycle progression, immune activation, extracellular matrix remodeling, cell migration, cell adhesion, and keratinocyte differentiation (Fig. 3B and table S3). Several of the 70 significantly enriched pathways were targeted by previous therapeutic approaches. For instance, fsEVs triggered differential regulation of ornithine metabolism and signaling, which has been a target of wound-healing therapies successfully evaluated in clinical studies (*33*, *34*). This further highlights the therapeutic means explored by wound-healing fsEVs and their parallels to previous wound-healing therapies. Therefore, these results are in good agreement with the functional analysis of fsEVs and reveal the central functional mechanisms by which the fibrocyte EV-inspired fsEVs promote wound healing.

To demonstrate the advantages of fsEVs for systematic decoding of EV signaling principles, RNA transcription analysis of keratinocyte cultures treated with fsEV with tetraspanin decoration but lacking any miRNAs was performed. We found 168 up-regulated and 63 down-regulated genes (table S4) as compared to cultures treated only with the lipid vesicles. Moreover, by applying different combinations of the three recombinant tetraspanin domains, we identified overlapping and unique DEGs triggered by the individual tetraspanins (Fig. 3C). A general "the whole is more than the sum of its parts" synergistic effect was observed. For instance, single presentation of CD9 and CD63 did not show any DEGs, while their combined presentation resulted in 10 DEGs (table S4). Moreover, we could draw direct correlations between the number of DEGs and the phenotypic effects observed in the functional analysis. For instance, our assessment of proliferation (see Fig. 2A) showed that CD81, presented alone or in combination with the other two tetraspanins, appears to have the most pronounced effect on proliferation. Similarly, CD81, presented alone or in combination, induced the highest number of DEGs. This concept of step-by-step component analysis can also be applied for the six miRNAs of the fsEVs, which we found to induce 57 DEGs, mostly enriched in pathways commonly associated with the citric acid cycle and mitochondrial respiration (see fig. S11 and tables S5 and S6). This showcases how fsEVs can be applied to decipher the contribution of individual EV components to specific changes in transcriptional profiles.

On the basis of this tetraspanin-resolved assessment, PEA revealed the particular phenotypic changes associated with the specific tetraspanin combinations (Fig. 3D and table S7). For instance, DEGs triggered by a combination of the recombinant human extracellular domains of CD9 and CD81 particularly enriched in pathway associated with immune regulation. Furthermore, this tetraspanin-resolved approach allowed us to draw correlations between the functional effects of specific fsEV formulations and associated transcriptomic changes, elucidating how specific EV constituents exert their phenotypic effects, while others remain ineffective. To exemplify this, we focused on DEG patterns in type I hemidesmosome assembly. We found that only certain tetraspanin combinations induce down-regulation of the central desmosome complex units, revealing how the individual tetraspanins contribute to hemidesmosome disassembly, a pivotal requirement for proper wound healing (Fig. 3E) (*35*). Together, breaking down the complexity of EVs by means of the fsEV technology in combination with transcriptomic profiling allowed us to uncover previously inconceivable quantitative insights into the functional mechanisms of EV signaling.

fsEVs for regenerative therapies

Beyond the scope of wound healing, exosomes derived from mesenchymal cells (e.g., fibrocytes) have raised significant therapeutic interest for several regenerative therapies, particularly ameliorating vascular remodeling and neovascularization in myocardial infarction and stroke therapy (*36*–*38*). Tissue vascularization is playing a crucial role in proper physiological supply of injured and healthy tissues, wherefore we aimed to assess the potential of fsEVs to promote neovascularization in developing tissue architectures. Toward this end, we applied a cell accumulation technique (*39*) for construction of three-dimensional (3D) vascularized multilayered organotypic connective tissues harboring human umbilical vein endothelial cells (HUVECs) and assessed tissue vascularization by immunofluorescence imaging (Fig. 4A and movie S2). These organotypic tissues were treated either with fsEVs or with buffer and the soluble fsEV constituents (proteins and miRNAs) as controls. Quantification of the mature vasculature after 7 days of tissue development by confocal microscopy showed that fsEVs significantly enhanced the total vasculature length and the interconnectivity (e.g., vessel junctions) between the vessel (Fig. 4B). This demonstrates that fsEVs hold the potential of mesenchymal-derived EVs to augment neovascularization of tissues. Moreover, it highlights that fsEVs are able to support fundamental tissue rearrangements and patterning, which is of pivotal importance in a wide variety of research fields with a therapeutic context.

DISCUSSION

In conclusion, the presented achievements represent a major milestone for bottom-up synthetic biology, opening doors for previously unknown approaches in applied and fundamental research. We have succeeded in the design and assembly of programmable fsEVs, which are accurately mimicking the functionalities of natural EVs using a complementary synthetic biology approach to integrate these synthetic constructs

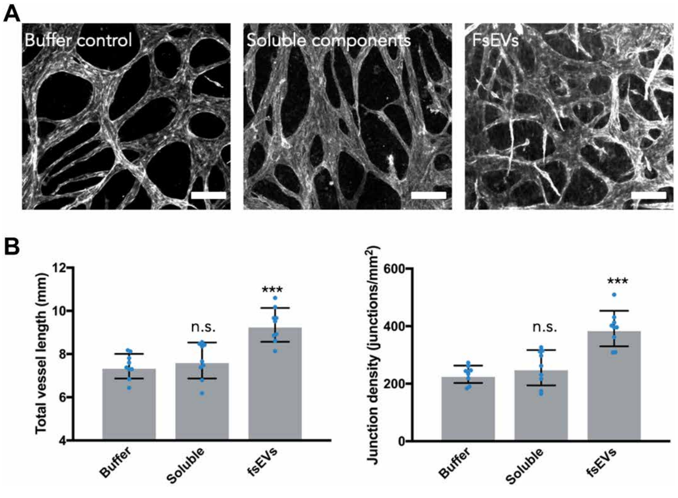

Fig. 4. fsEVs promoted neovascularization within organotypic tissues. (**A**) Confocal microscopy maximal *z*-projection of anti-CD31–stained multilayered fibroblast tissues harboring HUVECs 7 days after tissue formation. Tissues were treated with phosphate-buffered saline as buffer control, the soluble protein and miRNA components or fsEVs. Scale bars, 100 μm. (**B**) Quantification of the vasculature from tissues in (A). Results are shown as means ± SD from nine single z-stacks. $^{***}P < 0.0001$, two-tailed *t* test. n.s., not significant to the buffer treatment group.

with living biological systems. Future preclinical in vivo assessments could not only analyze the impact of fsEVs on advanced wound-healing processes (e.g., angiogenesis or scar formation) but also provide direct wound-side comparisons between natural and synthetic EVs. Looking toward the application of EVs in a clinical context, we have identified key miRNA and protein compositions at a quantitative level, which overcome the technological challenges related to EV isolation and purification from natural sources. The developed approach allows the design and production of functional EVs based on a bioinspired blueprint and may move the boundaries of EV therapy beyond the limits of bioderived EVs. More broadly, our technology has the potential to bring forward an entirely new class of therapeutics based on merging synthetic, lifelike assemblies and living systems. Such platforms could further be used to accurately explore the principal biophysical mechanisms on which EV functions rely.

MATERIALS AND METHODS

Materials

The following were purchased from Avanti Polar Lipids, USA: 18:1 1,2-dioleoyl-sn-glycero-3-phospho-(1′-rac-glycerol) (DOPG); 18:1 1,2-dioleoyl-sn-glycero-3-phosphocholesteroline (DOPC); 18:1 1,2-dioleoyl-sn-glycero-3-phosphoethanolamine (DOPE); 1,2-dioleoyl-sn-glycero-3-phosphoethanolamine-*N*-(lissamine rhodamine B sulfonyl) (Liss Rhod PE); 18:1 1,2-dioleoyl-sn-glycero-3-[(*N*-(5-amino-1-carboxypentyl)iminodiacetic acid)succinyl] (nickel salt) [DGS-NTA(Ni)]; 18:1 1,2-dioleoyl-sn-glycero-3-phospho-(1′-myo-inositol) (ammonium salt); 18:1 1,2-di-(9Z-octadecenoyl)-sn-glycero-3-phospho-L-serine (sodium salt); 18:1 1,2-di-(9Z-octadecenoyl)-sn-glycero-3-phosphate (sodium salt), cholesterol; 18:1 1-2-di-(9Z-octadecenoyl)-sn-glycerol; 18:0 *N*-stearoyl-D-erythro-sphingosylphosphorylcholine; and extrude set with 50-nm pore size polycarbonate filter membranes. All lipids were stored in chloroform at −20°C and used without further purification. Hoechst 33342, CellTracker Green 5-chloromethylfluorescein diacetate (CMFDA) dye, wheat germ agglutinin (WGA) Alexa Fluor conjugates, Dulbecco's modified Eagle's medium (DMEM) high glucose, heat-inactivated and exosome-depleted fetal bovine serum, penicillin-streptomycin (10,000 U/ml), L-glutamine (200 mM), Vybrant DiI Cell-Labeling Solution, Alexa Fluor 488 *N*-hydroxysuccinimide (NHS) Ester, anti-mouse Alexa Fluor 594, trypsin-EDTA (0.05%) with phenol red, and phosphate-buffered saline (PBS) were purchased from Thermo Fisher Scientific, Germany. 1*H*,1*H*,2*H*,2*H*-perfluoro-1-octanol (PFO) de-emulsifier, transwell cell culture inserts, ammonium acetate for MS, eluent additive for liquid chromatography–MS (LC-MS), gelatin from bovine skin, and human male serum were purchased from Sigma-Aldrich, Germany. Bovine albumin fraction V [bovine serum albumin (BSA)] and water Rotisolve were purchased from Carl Roth, Germany. HaCaT cells were obtained from CLS Cell Line Service, Germany. BJ cell lines and Iscove's modified Dulbecco's medium were obtained from the American Type Culture Collection, USA. Atto 488–conjugated 1,2-dipalmitoyl-sn-glycero-3-phosphoethanolamine was purchased from ATTO-TEC GmbH, Germany. Recombinant N-terminal His-tagged human CD9 (amino acids 112 to 195) was purchased from Sino Biological, Germany. HUVEC cells were purchased from Lonza, Switzerland. Recombinant N-terminal His-tagged human TSG101 (amino acids 1 to 145) was purchased from Fitzgerald, USA. Recombinant N-terminal His-tagged human CD81 (amino acids 113 to 201) was purchased from MyBioSource, USA. miRIDIAN miRNA mimics (hsa-miR-21-5p, hsa-miR-124-3p, hsa-miR-125b-5p, hsa-miR-126-5p, hsa-miR-130a-3p, and hsa-miR-132-3p) were purchased from Horizon Dharmacon, USA. K562 exosomes (HBM-K562) were obtained from HansaBioMed/Lonza, Switzerland. Four-well cell exclusion inserts were purchased from ibidi, Germany. Endothelial cell growth medium was purchased from PromoCell, Germany. Prewounded full-thickness human organotypic skin cultures, respective culture media, and histological sample preparation services were purchased from MatTek Cooperation, USA. Normal human dermal fibroblasts (NHDFs) were isolated at the Department of Dermatology, Uniklinik Aachen from the foreskin or specimens from cutaneous surgery in healthy subjects after informed consent and according to the institutional guidelines and the Declaration of Helsinki principles. The approval for this was granted by the ethics committee of University Hospital, RWTH Aachen, Germany. FC-40 oil was purchased from IoLiTec, Germany. The ELISA kit for the quantification of human pro–collagen Iα and anti-CD31 (ab9498) was obtained from Abcam, UK. Methanol LC-MS CHROMASOLV (≥99.9) was purchased from Honeywell/Riedel-de Haën. Fibronectin was purchased from Santa Cruz Biotechnology, USA. Dichloromethane SupraSolv for gas chromatography MS was purchased from Merck Millipore.

Methods

Confocal and bright-field microscopy

Following the procedures previously described in (*10*), we performed confocal microscopy with a laser-scanning microscope (LSM 800, Carl Zeiss AG). Images were acquired with a 20× (Objective Plan-Apochromat 20×/0.8 M27, Carl Zeiss AG) and a 63× immersion oil objective [Plan-Apochromat 63×/1.40 oil DIC (differential interference contrast), Carl Zeiss AG]. Images were analyzed with ImageJ National Institutes of Health (NIH)], and adjustments to image brightness and contrast as well as background corrections were always performed on the whole image and special care was taken not to obscure or eliminate any information from the original image. For bright-field imaging, a Leica DMi8 inverted fluorescent microscope equipped with an sCMOS (scientific complementary metal-oxide semiconductor) camera and 10× HC PL FLUOTAR (numerical aperture 0.32, PH1) objective was used.

For analysis of fsEV uptake into HaCaT cells, rhodamine B–labeled fsEVs were incubated with HaCaT cells in Nunc LabTek eight-well chambers. Immediately after addition of the fsEVs to the cells, Alexa Fluor–conjugated WGA (5 μg/ml) was added to the medium. Cells were incubated for 24 hours and subsequently imaged by confocal laser scanning microscopy. WGA binds to specific sugar residues on the outer cell membrane and is endocytosed along with these during membrane turnover and endocytotic processes, thereby staining intracellular endosomal vesicles. Alexa Fluor 488–labeled CD9 was produced by incubating NHS-functionalized Alexa Fluor 488 with recombinant CD9 in a twofold molar excess for 2 hours at 37°C in PBS. Subsequently, free NHS was quenched by adding a 10-fold molar excess of glycine. Staining of HaCaT cells with CellTracker Green was performed by incubating 20 μM CellTracker Green CMFDA dye for 60 min. To remove excess dye and non-uptaken fsEVs, cells were rinsed twice with PBS.

Cell culture

HaCaT and BJ cells were cultured in DMEM supplemented with glucose (4.5 g/liter), 1% L-glutamine, 1% penicillin/streptomycin, and 10% fetal bovine serum. Cells were routinely cultured at 37°C and 5% CO_2 atmosphere and passaged at ~80% confluency based on 0.05% trypsin/EDTA treatment. K562 cells were cultured in suspension in Iscove's modified Dulbecco's medium supplemented with 10% exosome-free fetal bovine serum. K562 cells were split every other day by transferring 3 ml of cell suspension to 10 ml of fresh cell culture medium.

Assessment of cell proliferation

To assess proliferation, we used a previously published Hoechst 33342 intensity analysis (*27*). To this end, HaCaT cells were seeded at a density of 15,000 cells per well in a flat-bottom transparent 96-well plate in 200 μl of culture medium. Cells were seeded together with corresponding fsEV vesicles and incubated for 48 hours. Subsequently, cells were washed twice with 100 μl of PBS and incubated for 10 min in ice-cold culture medium supplemented with 10 μM Hoechst 33342. After removal of the culture medium and 2× washing with PBS, Hoechst 33342 intensity was measured at four different positions in each well using an Infinite M200 TECAN plate reader controlled by TECAN iControl software with an in-built gain optimization and excitation/emission setting adjusted to 380/460 nm. Measurements were performed in triplicates.

Quantification of fsEV-to-cell attraction

Following the procedures previously described in (*10*), we assessed attraction between cells and fsEVs as well as their uptake by seeding HaCaT cells in triplicates in 100 μl of growth medium in flat-bottom 96-well plates and incubating them to form a confluent monolayer after 24 hours. fsEVs (labeled with Liss Rhod PE lipids) were added to a final lipid concentration of 1.5 μM and incubated for 24 hours. Fluorescence intensity in each well was quantified using an Infinite M200 TECAN plate reader controlled by TECAN iControl software with an in-built gain optimization and excitation/emission setting adjusted to 550/585 nm. Subsequently, wells were washed three times with 100 μl of PBS to remove unbound and non-uptaken fsEVs using a multichannel pipette followed by another measurement to quantify residual fluorescence in each well. To account for any variation in sample preparation, fluorescence intensity after washing was normalized to the fluorescence intensity before washing. All measurements were performed in triplicates at four different positions per well to account for variations in cell monolayer density.

Cell exclusion assay

For in vitro 2D wound-healing assays, four-well silicone cell exclusion cell culture inserts with a gap width of 500 μm were used in 12-well plastic plates. Cells were seeded at a cell density of 40,000 cells per well and allowed to adhere overnight in 110 μl of culture medium (2 ml of culture medium was added to the well outside the inserts). fsEVs were added with a final lipid concentration of 10 μM and incubated with the cell monolayer for 24 hours. Subsequently, the inserts were carefully removed using sterile tweezers and the wound was allowed to close for 16 hours. For quantification, the culture medium was removed and cell layers were fixed with ice-cold 4% paraformaldehyde (PFA) for a minimum of 20 min. The wound sites were analyzed using phase-contrast microscopy, and the cell-free area was quantified manually with ImageJ software.

Organotypic dermal cultures

For analysis of human organotypic full-thickness skin models, prewounded, single-donor, neonatal-foreskin tissue-derived normal human epidermal keratinocyte and fibroblast 3D cultures were obtained from a commercial distributor (MatTek Corporation). Skin models were cultured at an air-liquid interface following the manufacturer's recommendations. For wound closure analysis, tissues were allowed to equilibrate for 16 hours after adjusting to 37°C in a 5% CO_2 atmosphere. Subsequently, 2 μl (1 μM final lipid concentration) of the fsEV-containing solution (or respective buffer controls) was pipetted onto the wound site and the wound was allowed to heal for 48 hours at 37°C in a 5% CO_2 atmosphere. Tissues were then fixed with 10% formalin solution overnight at 4°C. Wound size was quantified from histological H&E slices. Six slices of three individual wounds each were analyzed. For quantification of the cell layer thickness of the regenerated epidermis, the epidermal thickness was measured at a 100-μm distance from the wound periphery (the epidermal tip in the cross-sectional H&E slides) with ImageJ software (NIH, USA).

Protein analysis by gel electrophoresis

A NuPAGE bold bis-tris 4 to 12% gradient gel with MES running buffer was used for a gel electrophoretic analysis of the protein spectrum contained in K562 exosomes and fsEVs. Electrophoresis was performed at 200 V for 35 min under denaturing conditions with a total of 3 μg and 500 ng of protein from fsEVs and natural exosomes, respectively, loaded onto separate lanes. Protein staining was performed with Coomassie R250 following a previously published method (*40*). Line intensity profiles of the respective lanes were measured by ImageJ software.

Production of fsEVs

fsEVs were produced from droplet-stabilized GUVs (dsGUVs) by shear stress emulsification following a previously published protocol (*6*–*8*). Briefly, a fluorosurfactant-containing FC-40 oil phase was added at a 2:1 ratio to a water phase containing SUVs as well as, in some cases, miRIDIAN RNAs. A triblock PEG2500-PFPE600-PEG2500 surfactant at a final concentration of 1.25 mM was used. For SUV production, lipids dissolved in chloroform stock solutions were mixed at the desired lipid ratio in glass vials and subsequently dried under a gentle nitrogen stream. The obtained lipid film was rehydrated to a final lipid concentration of 6 mM in PBS (+10 mM $MgCl_2$) for 15 min and afterward shaken for 5 min at 1000 rpm. This liposome solution was extruded at least nine times through a 100-nm pore size filter. For dsGUV production, the SUV solution was diluted to a final concentration of 3 mM with only PBS (+10 mM $MgCl_2$) or PBS (+10 mM $MgCl_2$) containing the desired miRNA components. This aqueous phase was added to the oil phase and emulsified using an ULTRA TURRAX IKA T10 basic emulsifier for 60 s at approximately 26,300 rpm. The resulting dsGUVs were incubated for at least 2 hours at 4°C in the dark. Release of the dsGUVs into an aqueous release buffer was performed by removing excess oil phase and adding PBS and PFO to the droplet mixture at a 1:1:1 ratio of aq. production buffer:aq. release buffer:PFO. After 30 min of equilibration, the GUV-containing layer was transferred into a 2-ml microtube, and PBS was added to obtain a final volume of 2 ml. This solution was centrifuged at >10,000*g* for 15 min. The supernatant was discarded, and the GUV pellet was resuspended in PBS.

The total lipid concentration of the GUV solution was determined by quantifying the fluorescence from the integrated rhodamine B or Atto 488–conjugated lipids, which was referenced to an SUV standard dilution curve. For coupling CD peptides, the total amount of NTA-$Ni2^+$–coupled lipids was calculated from the lipid ratio. The His-tagged peptides were added to the GUV solution in excess at a ratio of 1:2 and allowed to couple for 1 hour at 37°C protected from light. The GUV solution was subsequently centrifuged at >10,000 rpm for 15 min. The supernatant containing unbound peptides was removed, and the GUV pellet was resuspended in PBS. miRIDIAN miRNA mimics were always used at a concentration of 145 nM for dsGUV production.

For analysis of fsEV formation, dsGUV was produced from SUV containing 41 mole percent (mol %) cholesterol, 16 mol % N-acetyl-D-erythro-sphingosylphosphorylcholine (SM), 15 mol % DOPC, 11 mol % 1,2-dioleoyl-sn-glycero-3-phospho-L-serine(DOPS), 6 mol % DOPE, 5 mol % DOPG, 2 mol % 1,2-dioleoyl-sn-glycero-3-phosphate (PA), 1 mol % 1-2-dioleoyl-sn-glycerol (DAG), 1 mol % 1,2-dioleoyl-sn-glycero-3-phospho-(1′-myo-inositol) (PI), 1 mol % Liss Rhod PE, and 1 mol % DGS-NTA(Ni^{2+}) in PBS containing miRIDIAN RNA. After release into PBS containing 0.1% BSA (to block unspecific protein-lipid interactions), Alexa Fluor 488–labeled CD9 and 500 nM Hoechst 33342 were added to the GUVs for subsequent confocal microscopy analysis. For fsEV production, a total of 40 nM of miRIDIAN mimics was used.

Dynamic light scattering

Size and zeta potentials of fsEVs were measured with a Malvern Zetasizer Nano ZS system at a total lipid concentration of 15 μM in PBS. Temperature equilibration time was set to 300 s at 25°C followed by three repeat measurements for each sample at a scattering angle of 173° using the built-in automatic run-number selection. The material refractive index for fsEVs was set to 1.4233 and solvent properties to $\eta = 0.8882$, $n = 1.33$, and $\varepsilon = 79.0$.

EV isolation from K562 cell cultures

K562 EVs were isolated from conditioned cell culture medium by differential centrifugation. For this, K562 cells were cultured for 48 hours in suspension in 50 ml of Iscove's modified Dulbecco's medium containing 10% exosome-free serum at 37°C and 5% CO_2 atmosphere. The final cell concentration was 5×10^5 cells/ml. After incubation, the cell suspension was centrifuged at 300*g* at 4°C for 10 min to remove the cells. The supernatant was filtered through a 0.22-μm filter and centrifuged at 100,000*g* at 4°C for 75 min with a Beckmann Coulter Optima XE-100 ultracentrifuge in a JA-20 fixed angle rotor (k-factor 770). The pellet was washed with 50 ml of ice-cold PBS and centrifuged again under the same conditions. The EV pellet was resuspended in 1 ml of PBS. The total protein concentration of this EV suspension was assessed by measuring the absorbance at 280 nm with a NanoDrop ND-1000 spectrophotometer. For fluorescence EV staining with DiI (1,1′-dioctadecyl-3,3,3′,3′-tetramethylindocarbocyanine perchlorate), Vybrant DiI cell-labeling solution was diluted 1:1000 with the isolated EV solution for 15 min at room temperature (RT) in the dark. This solution was then recentrifuged at 100,000*g* at 4°C for 75 min. The EV pellet was resuspended in 1 ml of PBS.

Quantitative assessment of collagen deposition

For quantification of in vitro collagen deposition, BJ dermal fibroblasts were seeded in 96-well flat bottom transparent cell culture plates at a density of 20,000 cells per well. Twenty-four hours after seeding, cells were washed twice with PBS. Next, 200 μl of fresh cell culture medium was added to the cells together with the fsEVs (to reach a final lipid concentration of 10 μM). Cells were incubated for

Table 1A. Ionization, precursor selection, and fragmentation parameters for lipids monitored using LC-MS. CUR, curtain gas; TEM, temperature; GS1, nebulizer gas; GS2, heater gas; CAD, collision gas; IS, ionization voltage; DP, declustering voltage; CE, collision energy; CXP, cell exit potential; *m/z*, mass/charge ratio.

A: Source and ionization parameters			**B: MRM parameters**							
	+ Polarity	**– Polarity**	**Q1 (*m/z*)**	**Q3 (*m/z*)**	**Dwell time (ms)**	**ID**	**DP (V)**	**EP (V)**	**CE (V)**	**CXP (V)**
CUR (psi)	35	35	786.5	281.3	25	18:1 PS	–120	–10	–55	–8.5
TEM (°C)	180	600	753.4	288.3	20	15:0-18:1(d7) PS	–100	–10	–56	–10
GS1 (psi)	70	70	699.5	281.3	25	18:1 PA	–160	–10	–46	–9
GS2 (psi)	60	60	666.4	288.3	20	15:0-18:1(d7) PA	–170	–10	–46	–10
CAD	9	9	861.4	281.3	25	18:1 PI	–185	–10	–60	–11
IS (V)	5500	–4500	828.4	288.3	20	15:0-18:1(d7) PI	–90	–10	–60	–11
			773.4	281.3	25	18:1 PG	–135	–10	–52	–11
			741.4	289.3	20	15:0-18:1(d7) PG	–100	–10	–48	–10
			844.5	281.3	25	18:1 PC	–90	–10	–54	–7
			812.5	289.3	20	15:0-18:1(d7) PC	–115	–10	–50	–11
			404.3	369.4	100	Cholesterol	121	10	13	12
			411.2	376.3	60	Cholesterol (d7)	121	10	13	12
			731.6	184.1	20	18:0 SM	120	10	34	5.4
			739.5	185.0	20	d18:1-18:1(d9) SM	130	10	37	16
			638.5	339.3	20	18:1 DAG	50	10	27	12
			605.5	299.2	20	15:0-18:1(d7) DAG	91	10	21	6
			744.5	603.5	20	18:1 PE	92	10	33	16
			711.4	570.5	20	18:1 (d7) lyso PE	120	10	30	12

Table 1B. Sample specification for the RNA sequencing analysis of fully equipped fsEVs.

Sample A	Untreated HaCaT cells
Sample B	HaCaT cells treated with fsEVs harboring recombinant human ED2 of CD9, CD63, and CD81 as well as hsa-miR-21, hsa-miR-124, hsa-miR-125, hsa-miR-126, hsa-miR-130, and hsa-miR-132
Sample C	HaCaT cells treated with soluble forms of recombinant human ED2 of CD9, CD63, and CD81 as well as hsa-miR-21, hsa-miR-124, hsa-miR-125, hsa-miR-126, hsa-miR-130, and hsa-miR-132 at the same final concentration as in C

Table 2. Sample specification for the RNA sequencing analysis of differently equipped fsEVs.

Sample A	HaCaT cells treated with the fsEVs without any protein or miRNA components (lipid constituents only)
Sample B	HaCaT cells treated with fsEVs harboring recombinant human ED2 of CD9, CD63, and CD81 as well as hsa-miR-21, hsa-miR-124, hsa-miR-125, hsa-miR-126, hsa-miR-130, and hsa-miR-132
Sample C	HaCaT cells treated with fsEVs harboring recombinant human ED2 of CD9
Sample D	HaCaT cells treated with fsEVs harboring recombinant human ED2 of CD63
Sample E	HaCaT cells treated with fsEVs harboring recombinant human ED2 of CD81
Sample F	HaCaT cells treated with fsEVs harboring recombinant human ED2 of CD9 and CD63
Sample G	HaCaT cells treated with fsEVs harboring recombinant human ED2 of CD9 and CD81
Sample H	HaCaT cells treated with fsEVs harboring recombinant human ED2 of CD63 and CD81
Sample I	HaCaT cells treated with fsEVs harboring recombinant human ED2 of CD9, CD63, and CD81
Sample J	HaCaT cells treated with fsEVs harboring recombinant human ED2 of CD9, CD63, and CD81 as well as hsa-miR-21, hsa-miR-124, hsa-miR-125, hsa-miR-126, and hsa-miR-130

24 hours with fsEVs. Subsequently, human pro–collagen Iα was quantified in the medium by ELISA (ELISA Kit, Abcam) following the manufacturer's instructions.

Determination of lipid ratios

Lipid ratios were confirmed by multireaction monitoring (MRM) experiments using a Sciex QTrap 4500 system with a Shimadzu Nexera UPLC front-end system set up for flow injection analyses (FIAs). The Analyst 1.7.0 software from Sciex was used for instrument control.

FIA-MS–based lipid analysis can be affected by the effects of aggregation, adsorption, and suppression. Therefore, the use of heavy isotope-labeled internal standards is a necessity to ensure precise and reproducible results. For LC-MS experiments, we monitored lipids with nine different head groups. The Avanti SPLASH LIPIDOMIX Mass Spec Standard contained representative deuterated lipids, which covered all the chosen head groups. This internal standard mix was diluted 1:100 in 98% dichloromethane (DCM)/MeOH aq. + 10 mM NH_4Ac (50:50 v/v, LC-MS grade) and afterward used to dilute the calibrator and samples. An unprocessed PBS sample featuring the target lipid ratios (see fig. S3) was diluted 1:10,000, 1:5000, and 1:2500 and used for calibration and normalization. Samples were sonicated for 3 min and subsequently diluted 1:5000. The calibrator and sample dilutions were injected either in triplicates or in quintuplicates into a stream of 98% MeOH aq. (450 μl/min) + 10 mM NH_4Ac with air gaps of 0.1 μl.

The measurements were performed in negative and positive ionization mode (see Table 1A). Cholesterol showed increasing signal intensities with decreasing ion source temperature. Hence, for positive mode ionization, the temperature was lowered to 180°C. Lipid precursors were isolated as either de-/protonated or NH_4Ac-derived adducts. The selected precursors and MS2 fragments for MRM measurements along with their optimized parameters are given in Table 1B. Because of unequal concentrations and ionization efficiencies of the Avanti SPLASH LIPIDOMIX Mass Spec Standard lipids, the initial PG-d7, PC-d7, and SM-d9 signal intensities were found to be susceptible to detector saturation effects. To prevent these, the second isotopes of 15:0-18:1(d7) PG, 15:0-18:1(d7) PC, and d18:1-18:1(d9) SM were chosen as MRM precursors.

The recorded data were analyzed using the MultiQuant 3.0.2 software from Sciex. A 1.0- to 1.5-point Gaussian smooth was applied to data preceding the integration of MRM traces. A quadratic regression was used after integration. Quintuplicate injections of the diluted calibrator (1:5000) resulted in coefficients of variation (CV) of <4% except for 18:1 PI, the lipid with the lowest abundance, which had a CV of 7.45%.

Formation of multilayered vascularized tissues

Individual NHDFs were exposed alternatingly to fibronectin (0.04 mg/ml) and gelatin (0.04 mg/ml) with intermediate PBS washing steps as previously described (*39*). After nine steps of the coating process, 1×10^6 NHDFs were mixed with 1×10^5 HUVECs in a ratio of 10:1 together with (i) fsEVs (10 μM final lipid concentration), (ii) the soluble miRNAs and proteins, or (iii) PBS in media. This cell mixture was pipetted on top of 24-well cell culture inserts (0.4-μm pore size, 6.5-mm diameter) precoated with fibronectin. The cells were incubated for 3 hours in 300 μl of media (endothelial growth media:DMEM at a 1:1 ratio) with ascorbic acid (50 μg/ml) (Sigma-Aldrich) in the upper compartment and 1 ml of the same media on the lower compartment of the culture insert. After 3 hours of incubation (37°C, 5% CO_2), 1 ml of additional medium was added to connect the media of the lower compartment with the upper.

The assembled tissue was cultured for 7 days (37°C, 5% CO_2) with a change of media every other day. Fibronectin/gelatin-coated cells accumulate to form thick vascularized scaffold-free connective tissues (*41*, *42*).

Immunostaining and confocal microscopy of vascularized tissues

On day 7, the tissues were harvested, washed with PBS, and fixed with 4% PFA in PBS for 20 min. After PBS washing (three times, 5-min interval), tissues were incubated with 0.1% Triton X-100 for 15 min followed by 3% BSA for 2 hours at RT. After further PBS washing, tissues were incubated with mouse anti-CD31 primary antibody (1:50) at 4°C overnight. The next day, tissues were washed with PBS (three times, 5-min interval) and incubated with anti-mouse Alexa Fluor 594 antibody (1:100) at RT for 2.5 hours. Tissues were washed thoroughly and prepared for microscopy. Stained specimens were observed using confocal laser scanning microscopy (Leica TCS SP8). The samples were excited using a 561-nm diode-pumped solid-state laser (Alexa Fluor 594), and the emission was detected with HyD detectors. Samples were observed for vessels (CD31) with 20× oil objective, and the z-stacked images were taken at a resolution of 1024 × 1024 pixels. Images were processed in ImageJ software, and the vessel area, junction points, and vessel length were quantified using the semiautomatic AngioTool software (*43*).

RNA sequencing transcriptome analysis

For transcriptome profiling by RNA sequencing, 500,000 HaCaT keratinocytes were seeded into 12-well plates and cultured for 24 hours with 1 ml of culture medium. Afterward, fsEVs were added to a 30 μM final lipid concentration and incubated for 24 hours. As control conditions, cells were treated either with the soluble fsEV components or with PBS. Well plates were subsequently transferred on ice and washed 2× with ice-cold PBS. Then, the cell layers were scraped off with a spatula in 1 ml of ice-cold PBS. The 1-ml solution was transferred into 2-ml microcentrifuge tubes. To recover residual cells from the wells, an additional 1 ml of ice-cold PBS was added. This solution was also transferred to the microcentrifuge tubes, and the cells were subsequently pelleted at 13,000 rpm for 2 min. The supernatant was removed, and the cell pellets were snap-frozen in liquid nitrogen. All steps were performed whenever possible on ice.

The frozen pellets were shipped on dry ice to Genewiz (Germany) for RNA sequencing. The RNA sequencing workflow after RNA isolation included initial PolyA selection–based mRNA enrichment, mRNA fragmentation, and random priming with subsequent first- and second-strand complementary DNA (cDNA) synthesis. Afterward, end-repair 5′ phosphorylation and adenin nucleotide (dA)–tailing was performed. Last, adaptor ligation, polymerase chain reaction (PCR) enrichment, and Illumina NovaSeq technology–based sequencing with 2× 150–base pair (bp) read length were carried out. Trimmomatic v.0.36 software was applied to remove possible adaptor sequence reads and poor-quality nucleotide reads. Reads were aligned to the *Homo sapiens* GRCh38 reference genome available on ENSEMBL with STAR aligner v.2.5.2b. Unique gene hit counts were calculated with the feature counts from the Subread package v.1.5.2. The hit counts are reported based on the gene ID feature in the annotation file. Only unique reads that fall within exon regions were considered. The library preparation was strand specific; wherefore, reads were counted strand-specifically. DESeq was used for comparison of gene expression levels between the different sample groups. P values and $\log_2$ fold changes were calculated using the Wald test. Genes with an adjusted P value (P_{adj}) of <0.05 were referred to as DEGs. PEA was performed by analysis of the respective DEGs with the Reactome pathway Knowledgebase (*44*). The enrichment reports can be freely accessed under https://osf.io/qpr4j/?view_only=de4bb4d5c25e452a95171a1518896fe3.

Two RNA sequencing analyses were performed. The first analysis focused on the evaluation of DEGs between PBS-treated keratinocyte cultures and keratinocytes treated with fsEVs (composed of CD9, CD63, and CD81 as well as hsa-miR-21, hsa-miR-124, hsa-miR-125, hsa-miR-126, hsa-miR-130, and hsa-miR-132) or the respective soluble protein and miRNA compounds at the same final concentration. The second analysis focused on the comparison of DEGs between keratinocytes treated with vesicles lacking any protein or miRNA components and cells treated with fsEVs harboring different combinations of proteins and miRNAs. Technical specifications and quality reports can be accessed under https://osf.io/5tvk7/?view_only=f1998ad90ba444a39bb7a2337f1b29fa and https://osf.io/kwgam/?view_only=85f8a79e8135438d8f2e712f9d496f2b for the first and second analysis, respectively. Tables 1 and 2 summarize the sample specifications.

SUPPLEMENTARY MATERIALS

Supplementary material for this article is available at https://science.org/doi/10.1126/sciadv.abg6666

REFERENCES AND NOTES

1. S. C. Steenbeek, T. V. Pham, J. Ligt, A. Zomer, J. C. Knol, S. R. Piersma, T. Schelfhorst, R. Huisjes, R. M. Schiffelers, E. Cuppen, C. R. Jimenez, J. Rheenen, Cancer cells copy migratory behavior and exchange signaling networks via extracellular vesicles. *EMBO J.* **37**, e98357 (2018).
2. S. Aiello, F. Rocchetta, L. Longaretti, S. Faravelli, M. Todeschini, L. Cassis, F. Pezzuto, S. Tomasoni, N. Azzollini, M. Mister, C. Mele, S. Conti, M. Breno, G. Remuzzi, M. Noris, A. Benigni, Extracellular vesicles derived from T regulatory cells suppress T cell proliferation and prolong allograft survival. *Sci. Rep.* **7**, 11518 (2017).
3. L. Cruz, J. A. A. Romero, R. P. Iglesia, M. H. Lopes, Extracellular vesicles: Decoding a new language for cellular communication in early embryonic development. *Front. Cell Dev. Biol.* **6**, 94 (2018).
4. G. van Niel, G. D'Angelo, G. Raposo, Shedding light on the cell biology of extracellular vesicles. *Nat. Rev. Mol. Cell Biol.* **19**, 213–228 (2018).
5. S. El Andaloussi, I. Mäger, X. O. Breakefield, M. J. A. Wood, Extracellular vesicles: Biology and emerging therapeutic opportunities. *Nat. Rev. Drug Discov.* **12**, 347–357 (2013).
6. M. Weiss, J. P. Frohnmayer, L. T. Benk, B. Haller, J.-W. Janiesch, T. Heitkamp, M. Börsch, R. B. Lira, R. Dimova, R. Lipowsky, E. Bodenschatz, J.-C. Baret, T. Vidakovic-Koch, K. Sundmacher, I. Platzman, J. P. Spatz, Sequential bottom-up assembly of mechanically stabilized synthetic cells by microfluidics. *Nat. Mater.* **17**, 89–96 (2018).
7. B. Haller, K. Göpfrich, M. Schröter, J. W. Janiesch, I. Platzman, J. P. Spatz, Charge-controlled microfluidic formation of lipid-based single- and multicompartment systems. *Lab Chip* **18**, 2665–2674 (2018).
8. K. Göpfrich, B. Haller, O. Staufer, Y. Dreher, U. Mersdorf, I. Platzman, J. P. Spatz, One-pot assembly of complex giant unilamellar vesicle-based synthetic cells. *ACS Synth. Biol.* **8**, 937–947 (2019).
9. O. Staufer, M. Schroter, I. Platzman, J. P. Spatz, Bottom-up assembly of functional intracellular synthetic organelles by droplet-based microfluidics. *Small* **16**, e1906424 (2020).
10. O. Staufer, S. Antona, D. Zhang, J. Csatári, M. Schröter, J. W. Janiesch, S. Fabritz, I. Berger, I. Platzman, J. P. Spatz, Microfluidic production and characterization of biofunctionalized giant unilamellar vesicles for targeted intracellular cargo delivery. *Biomaterials* **264**, 120203 (2021).
11. G. Moreno-Pescador, C. D. Florentsen, H. Østbye, S. L. Sønder, T. L. Boye, E. L. Veje, A. K. Sonne, S. Semsey, J. Nylandsted, R. Daniels, P. M. Bendix, Curvature- and phase-induced protein sorting quantified in transfected cell-derived giant vesicles. *ACS Nano* **13**, 6689–6701 (2019).
12. I. Nakase, N. Ueno, M. Katayama, K. Noguchi, T. Takatani-Nakase, N. B. Kobayashi, T. Yoshida, I. Fujii, S. Futaki, Receptor clustering and activation by multivalent interaction through recognition peptides presented on exosomes. *Chem. Commun.* **53**, 317–320 (2017).
13. M. Arnold, E. A. Cavalcanti-Adam, R. Glass, J. Blümmel, W. Eck, M. Kantlehner, H. Kessler, J. P. Spatz, Activation of integrin function by nanopatterned adhesive interfaces. *ChemPhysChem* **5**, 383–388 (2004).

14. F. Lussier, O. Staufer, I. Platzman, J. P. Spatz, Can bottom-up synthetic biology generate advanced drug-delivery systems? *Trends Biotechnol.* **39**, 445–459 (2021).
15. T. Skotland, K. Sandvig, A. Llorente, Lipids in exosomes: Current knowledge and the way forward. *Prog. Lipid Res.* **66**, 30–41 (2017).
16. R. Vogel, A. K. Pal, S. Jambhrunkar, P. Patel, S. S. Thakur, E. Reátegui, H. S. Parekh, P. Saá, A. Stassinopoulos, M. F. Broom, High-resolution single particle zeta potential characterisation of biological nanoparticles using tunable resistive pulse sensing. *Sci. Rep.* **7**, 17479 (2017).
17. D. Kim, H. K. Woo, C. Lee, Y. Min, S. Kumar, V. Sunkara, H. G. Jo, Y. J. Lee, J. Kim, H. K. Ha, Y. K. Cho, EV-Ident: Identifying tumor-specific extracellular vesicles by size fractionation and single-vesicle analysis. *Anal. Chem.* **92**, 6010–6018 (2020).
18. J. Van Deun, P. Mestdagh, R. Sormunen, V. Cocquyt, K. Vermaelen, J. Vandesompele, M. Bracke, O. De Wever, A. Hendrix, The impact of disparate isolation methods for extracellular vesicles on downstream RNA profiling. *J. Extracell. Vesicles* **3**, (2014).
19. M. Y. Konoshenko, E. A. Lekchnov, A. V. Vlassov, P. P. Laktionov, Isolation of extracellular vesicles: General methodologies and latest trends. *Biomed. Res. Int.* **2018**, 8545347 (2018).
20. A. Geiger, A. Walker, E. Nissen, Human fibrocyte-derived exosomes accelerate wound healing in genetically diabetic mice. *Biochem. Biophys. Res. Commun.* **467**, 303–309 (2015).
21. M. Li, E. Zeringer, T. Barta, J. Schageman, A. Cheng, A. V. Vlassov, Analysis of the RNA content of the exosomes derived from blood serum and urine and its potential as biomarkers. *Philos. Trans. R. Soc. B Biol. Sci.* **369**, 20130502 (2014).
22. X. Osteikoetxea, A. Balogh, K. Szabó-Taylor, A. Németh, T. G. Szabó, K. Pálóczi, B. Sódar, Á. Kittel, B. György, É. Pállinger, J. Matkó, E. I. Buzás, Improved characterization of EV preparations based on protein to lipid ratio and lipid properties. *PLOS ONE* **10**, e0121184 (2015).
23. C. S. Stipp, T. V. Kolesnikova, M. E. Hemler, Functional domains in tetraspanin proteins. *Trends Biochem. Sci.* **28**, 106–112 (2003).
24. E. Lozano-Andrés, S. F. Libregts, V. Toribio, F. Royo, S. Morales, S. López-Martín, M. Valés-Gómez, H. T. Reyburn, J. M. Falcón-Pérez, M. H. Wauben, M. Soto, M. Yáñez-Mó, Tetraspanin-decorated extracellular vesicle-mimetics as a novel adaptable reference material. *J. Extracell. Vesicles* **8**, –1573052 (2019).
25. P. Boukamp, R. T. Petrussevska, D. Breitkreutz, J. Hornung, A. Markham, N. E. Fusenig, Normal keratinization in a spontaneously immortalized aneuploid human keratinocyte cell line. *J. Cell Biol.* **106**, 761–771 (1988).
26. S. N. Hurwitz, M. M. Conlon, M. A. Rider, N. C. Brownstein, D. G. Meckes Jr., Nanoparticle analysis sheds budding insights into genetic drivers of extracellular vesicle biogenesis. *J. Extracell. Vesicles* **5**, –31295 (2016).
27. D. F. Gilbert, G. Erdmann, X. Zhang, A. Fritzsche, K. Demir, A. Jaedicke, K. Muehlenberg, E. E. Wanker, M. Boutros, A novel multiplex cell viability assay for high-throughput RNAi screening. *PLOS ONE* **6**, e28338 (2011).
28. F. Berditchevski, E. Odintsova, Characterization of integrin-tetraspanin adhesion complexes: Role of tetraspanins in integrin signaling. *J. Cell Biol.* **146**, 477–492 (1999).
29. T. Shibue, R. A. Weinberg, Integrin beta1-focal adhesion kinase signaling directs the proliferation of metastatic cancer cells disseminated in the lungs. *Proc. Natl. Acad. Sci. U.S.A.* **106**, 10290–10295 (2009).
30. Y. M. Sun, K. Y. Lin, Y. Q. Chen, Diverse functions of miR-125 family in different cell contexts. *J. Hematol. Oncol.* **6**, 6 (2013).
31. M. Alexander, R. Hu, M. C. Runtsch, D. A. Kagele, T. L. Mosbruger, T. Tolmachova, M. C. Seabra, J. L. Round, D. M. Ward, R. M. O'Connell, Exosome-delivered microRNAs modulate the inflammatory response to endotoxin. *Nat. Commun.* **6**, 7321 (2015).
32. X. Yang, J. Wang, S.-L. Guo, K.-J. Fan, J. Li, Y.-L. Wang, Y. Teng, X. Yang, miR-21 promotes keratinocyte migration and re-epithelialization during wound healing. *Int. J. Biol. Sci.* **7**, 685–690 (2011).
33. C. Coudray-Lucas, H. Le Bever, L. Cynober, J. P. De Bandt, H. Carsin, Ornithine α-ketoglutarate improves wound healing in severe burn patients: A prospective randomized double-blind trial versus isonitrogenous controls. *Crit. Care Med.* **28**, 1772–1776 (2000).
34. I. B. J. G. Debats, N. E. P. Deutz, E. Vd Hogen, W. D. Boeckx, R. R. W. Vd Hulst, Ornithine pathway stimulated in human wound healing during arginine suppletion. *Clin. Nutr.* **22**, S30 (2003).
35. S. B. Hopkinson, K. J. Hamill, Y. Wu, J. L. Eisenberg, S. Hiroyasu, J. C. R. Jones, Focal contact and hemidesmosomal proteins in keratinocyte migration and wound repair. *Adv. Wound Care* **3**, 247–263 (2014).
36. C. Merino-González, F. A. Zuñiga, C. Escudero, V. Ormazabal, C. Reyes, E. Nova-Lamperti, C. Salomón, C. Aguayo, Mesenchymal stem cell-derived extracellular vesicles promote angiogenesis: Potencial clinical application. *Front. Physiol.* **7**, 24 (2016).
37. L. Huang, W. Ma, Y. Ma, D. Feng, H. Chen, B. Cai, Exosomes in mesenchymal stem cells, a new therapeutic strategy for cardiovascular diseases? *Int. J. Biol. Sci.* **11**, 238–245 (2015).
38. J. Chen, M. Chopp, Exosome therapy for stroke. *Stroke* **49**, 1083–1090 (2018).
39. A. Nishiguchi, H. Yoshida, M. Matsusaki, M. Akashi, Rapid construction of three-dimensional multilayered tissues with endothelial tube networks by the cell-accumulation technique. *Adv. Mater.* **23**, 3506–3510 (2011).
40. U. K. Laemmli, Cleavage of structural proteins during the assembly of the head of bacteriophage T4. *Nature* **227**, 680–685 (1970).
41. S. Singh, Y. Marquardt, R. Rimal, A. Nishiguchi, S. Huth, M. Akashi, M. Moeller, J. M. Baron, Long-term and clinically relevant full-thickness human skin equivalent for psoriasis. *ACS Appl. Bio Mater.* **3**, 6639–6647 (2020).
42. H. Miyazaki, Y. Tsunoi, T. Akagi, S. Sato, M. Akashi, D. Saitoh, A novel strategy to engineer pre-vascularized 3-dimensional skin substitutes to achieve efficient, functional engraftment. *Sci. Rep.* **9**, 7797 (2019).
43. E. Zudaire, L. Gambardella, C. Kurcz, S. Vermeren, A computational tool for quantitative analysis of vascular networks. *PLOS ONE* **6**, e27385 (2011).
44. B. Jassal, L. Matthews, G. Viteri, C. Gong, P. Lorente, A. Fabregat, K. Sidiropoulos, J. Cook, M. Gillespie, R. Haw, F. Loney, B. May, M. Milacic, K. Rothfels, C. Sevilla, V. Shamovsky, S. Shorser, T. Varusai, J. Weiser, G. Wu, L. Stein, H. Hermjakob, P. D'Eustachio, The reactome pathway knowledgebase. *Nucleic Acids Res.* **48**, D498–D503 (2020).

Acknowledgments: We thank A. Hellwig and H. Bading (Interdisciplinary Center for Neuroscience, University of Heidelberg) for support with TEM experiments. We are grateful to I. Kajzar (University Hospital Heidelberg), D. Missirlis, A. Cavalcanti-Adam, and N. Grunze (Max Planck Institute for Medical Research) for proofreading the manuscript. O.S. acknowledges support from the Heidelberg Bioscience International Graduate School and the Max Planck School Matter to Life. J.P.S. is the Weston Visiting Professor at the Weizmann Institute of Science and part of the excellence cluster CellNetworks at University of Heidelberg. O.S. is the Meurer Visiting Professor at University of Bristol. The Max Planck Society is appreciated for its general support. **Funding:** The authors acknowledge funding from the Federal Ministry of Education and Research of Germany, grant agreement no. 13XP5073A, PolyAntiBak, and the MaxSynBio Consortium, which is jointly funded by the Federal Ministry of Education and Research of Germany and the Max Planck Society. They also acknowledge the support from the Volkswagen Stiftung (priority call "Life?"). J.P.S. acknowledge funding from the Deutsche Forschungsgemeinschaft (DFG, German Research Foundation) under Germany's Excellence Strategy via the Excellence CLuster 3D Matter Made to Order (EXC-2082/1 - 390761711). **Author contributions:** O.S., I.P., and J.P.S. conceived the research, designed the experiments, and wrote the manuscript with input from all authors. I.P. and J.P.S. led the study and supervised the research. O.S. performed fsEV synthesis and in vitro characterization. F.D. and H.B. performed and analyzed experiments with organotypic human skin models. S.F. performed MS analysis. M.S. synthesized block-copolymer surfactants. R.R., S.S., and M.M. developed vascularization models and performed and analyzed neovascularization experiments. The final version of the manuscript was approved by all authors. **Competing interests:** The authors have filed a patent, European Patent Office PCT/EP2021/052145, related to the content of this study. The authors declare that they have no other competing interest. **Data and materials availability:** Synthesized surfactants were custom-made for this study and might show batch-to-batch variability. All data needed to evaluate the conclusions in the paper are present in the paper and/or the Supplementary Materials.

Submitted 20 January 2021
Accepted 14 July 2021
Published 3 September 2021
10.1126/sciadv.abg6666

Citation: O. Staufer, F. Dietrich, R. Rimal, M. Schröter, S. Fabritz, H. Boehm, S. Singh, M. Möller, I. Platzman, J. P. Spatz, Bottom-up assembly of biomedical relevant fully synthetic extracellular vesicles. *Sci. Adv.* **7**, eabg6666 (2021).